Ceramics International xxx (xxxx) xxx–xxx

Contents lists available at ScienceDirect

Ceramics International

journal homepage: www.elsevier.com/locate/ceramint

Characterization of alumina-magnesia-carbon refractory bricks containing aluminium and silicon

W.A. Calvo[a], P. Ortega[b], M.J. Velasco[b], V. Muñoz[a], P. Pena[b], A.G. Tomba Martinez[a,*]

[a] Instituto de Investigaciones en Ciencia y Tecnología de Materiales (INTEMA), CONICET-Facultad de Ingeniería/Universidad Nacional de Mar del Plata, Av. J.B. Justo 4302, 7600 Mar del Plata, Argentina

[b] Instituto de Cerámica y Vidrio (ICV), CSIC Kelsen 5, 28049 Madrid, España

ARTICLE INFO

Keywords:
D. Al_2O_3
D. MgO
D. Carbon
E. Refractories

ABSTRACT

The present paper is a continuation of previous ones focused on the characterization of alumina-magnesia-carbon refractories (AMC) bricks. Unlike those characterised materials which only have aluminium as an antioxidant, a brick also containing silicon is comparatively analysed in this paper. Along with metallic aluminium, silicon is among the most commonly used antioxidant additives in oxide-C refractories, but the studies on the incorporation of this metal into AMC bricks are rather limited.

In this work, several complementary techniques were used in combination to achieve a detailed characterization in relation to the physical and chemical characteristics and thermal evolution of the Si-containing AMC refractory: X-ray fluorescence, plasma emission spectroscopy, gravimetry, granulometry, X-ray diffraction, differential thermal and thermogravimetric analyses, reflection optical and scanning electron microscopies, mercury intrusion porosimetry, and density, porosity, permanent linear change and permeability measurements. In addition, the characterization was completed by evaluating the chemical resistance to air and to a basic slag and calculating the equilibrium composition of the brick when it is subjected to high temperatures (up to 1400 °C). A comparison with the results obtained for previously characterised AMC bricks with similar MgO contents and metallic aluminium as an antioxidant was also made. The presence of silicon was related to finer open porosity and higher oxidation resistance at high temperature (1400 °C).

1. Introduction

The present paper is a continuation of previous ones reported by the authors [1,2], in which results of the characterization of alumina-magnesia-carbon materials (Al_2O_3-MgO-C, AMC) were presented. The data generated in this type of research is fundamental to understanding the behaviour of the materials in service conditions (as was done in other papers by the authors), with the final aim of establishing what the determining factors are. With this information, brick design and performance can be enhanced.

AMC refractory bricks are used mainly on sidewalls and bottom working linings of steel-making ladles, a vessel with a critical role in current integrated metallurgical processes [3]. The application of AMC bricks in the slag line is limited due their susceptibility to basic melt attack at high temperature [4]. These refractories are exposed to severe mechanical and thermal loading throughout their lifetime, in an aggressive environment comprised of melts (metal and slag), gases and solid particles. Their main advantage with respect to the other members of the C-oxide family, such as MgO-C and Al_2O_3-C bricks, is the *in-situ* formation of $MgAl_2O_4$ spinel at temperatures over 1000 °C, an expansive process which collaborates to close joints, reducing the corrosion by melts.

Unlike previously characterised AMC refractories which only have aluminium as an antioxidant, a brick also containing silicon is comparatively analysed in this work. Along with metallic aluminium, silicon is among the most commonly used antioxidant additives due to its low cost. Several reports regarding the performance of Si in MgO-C refractories can be found in the literature [5–10], including its combination with other additives (usually Al). The use of Si in the specific field of AMC bricks, as well as studies on the incorporation of this metal into this type of refractories, are rather limited [11].

Metallic silicon has an advantage over aluminium since it doesn't possess the hydration disadvantages created by the formation of Al_4C_3, which is very sensible to humidity and tends to expand [12]. Moreover, it has been reported that the addition of silicon powders to Al_2O_3-C and bauxite-SiC reduces pore sizes, thus increasing the proportion of pores smaller than 1 μm and the mean pore size [12,13]; this aspect is critical in the material's resistance to gaseous and liquid fluid attack. The

* Corresponding author.
E-mail address: agtomba@fi.mdp.edu.ar (A.G.T. Martinez).

https://doi.org/10.1016/j.ceramint.2018.02.069
Received 31 January 2018; Accepted 7 February 2018

formation of solid phases such as silicon carbide (SiC) and forsterite (Mg_2SiO_4) by the reaction between Si and C and MgO, respectively, in the case of MgO-C refractories, enhances the hot mechanical properties [5,10]. However, according to Ghosh et al., the role of Si as an antioxidant begins from 1400 °C onwards and is less effective than that of Al [7]; this is because silicon does not generate gaseous species at low temperature (as Al does, which favours its dispersion and reactivity), and SiC is formed at temperatures higher than that required for Al_4C_3 formation.

In this work, the methodology used to characterise an AMC commercial brick used in the bottom of a steelmaking ladle and containing a combination of Si and Al as antioxidant additives is presented. The characterization involves physical, chemical, thermal, granulometric, microstructural and textural aspects. The presence of silicon required modifications to be made in the experimental strategy previously used, and new techniques were also applied, including the thermodynamic simulation of the material's thermal evolution. The results obtained were analysed, and a comparison was made with those of previously characterised AMC bricks with similar MgO contents and metallic aluminium as an antioxidant [1,2]. Finally, AMC refractories were analysed regarding their chemical resistance to air oxidation and basic slag corrosion, with the aim of finding the main factors which determine the differences in the behaviour of each brick.

2. Experimental procedure

This work is focused on the characterization of a commercial AMC brick, labelled as AMC4, which is used in the bottom of a ladle in a local steel shop. The methodology used in this case was analogous to that designed for the evaluation of AMC bricks with similar MgO contents (~ 5–7 wt%) and a phenolic resin as an organic binder (AMC1 and AMC3), containing only metallic aluminium as antioxidant [1,2], and whose results are contrasted with those obtained in the present work. However, some changes should be made to the methodological scheme when the presence of Si is detected in AMC4, and some other additional analytic techniques were also used:

Microstructure: reflected light optical microscopy (RLOM) and scanning electron microscopy coupled with X-ray energy dispersive spectroscopy (SEM/EDS) were used to analyse the nature of raw materials and their distribution in the granulometric fractions (coarse, medium-sized, fine).

Mineralogical composition: determined by qualitative X-ray diffraction (XRD) together with observations made by reflected light optical microscopy and scanning electron microscopy coupled with X-ray dispersive energy (SEM/EDS). The quantification of the main components was carried out by the rational analysis of the chemical analysis data, as was previously reported [1].

Chemical composition: an *ad-hoc* methodology described in a previous paper by the authors was used [1] that combines X-ray fluorescence (XRF), plasma emission spectroscopy (ICP-OES) and gravimetry to analyse powdered samples previously treated according to specific thermal schedules. Considering the composition of AMC4, some changes to the original methodology should be made.

Particle size distribution: the particle size distribution was determined in a different way, by sieving powders obtained by the thermal treatment of brick fragments (the treatment was performed to pyrolyze the binder and release the particles).

Texture: complementary techniques, such as measurements of global and picnometric densities, total, open and closed porosities and permeability, together with mercury intrusion porosimetry were used to characterise the pores. A different method to determine permeability was used in this case, also based on the flow of nitrogen gas.

Thermal evolution of phases: the specific changes taking place in the material when temperature increased were determined by differential thermal and thermogravimetric analyses (DTA/TGA) under oxidant atmosphere (air). In addition, thermal treatments were carried out in air on brick fragments in order to take into account the effect of texture and then, XRD was performed on powdered samples of the treated bodies. These results were compared with the equilibrium composition of AMC4 at temperatures up to 1400 °C, which was calculated by computational simulation using FactSage software (V.7.1).

Permanent linear change: the residual expansion of AMC refractories is one of the key properties of this type of materials. The permanent dimensional change (PLC) of the brick with respect to temperature was evaluated in air up to 1400 °C. Additionally, measurements of the bulk density and global porosity were performed after each cycle in order to follow their evolution.

Oxidation resistance: the refractory's sensitivity to an oxidant atmosphere (air) due to the presence of carbon was evaluated by static thermal treatments of specimens up to 1400 °C; the mass variation and the size of the decarburized (discoloured) area were used as indicators of the loss of carbon by oxidation.

Slag corrosion resistance: the cup static test was employed to determine the resistance of the refractory to be attacked by a molten basic slag at 1450 °C, in air; material wear was used as an indicator of the degree of corrosion.

2.1. Experimental techniques

Powdered samples and specimens representative of AMC4 bricks were used for the analysis.

The powdered samples were prepared from a batch (~ 200 g) of fragments of the refractory brick. Firstly, a coarse grinding was performed (manually) up to a granulometry suitable for manipulation (< 1 cm). Then, a finer grinding was carried out in a planetary mill (Planetary - Micro Mill “Pulverisette 7” Fritsch) at 595 rpm for intervals of 5 min until obtaining the particle size required for each of the analytical techniques (between 75 and 120 μm). For the hardest components corresponding to alumina aggregates, manual grinding using an impact mortar of tungsten carbide was necessary. When the sample was completely reduced to the required particle size, it was successively quartered.

The specimens used in the different tests were cut from the brick using diamond-cutting disks and diamond drills. In some cases, the specimens were impregnated in polyester resins in vacuum to prepare surfaces for microstructural analysis by cut and grinding. These surfaces were sequentially ground with SiC paper up to 4000 grit, with isopropanol as a lubricant. For the final polishing, diamond pastes up to 1 μm were used.

The reflected light optical microscopy (RLOM) was carried out on the polished surfaces using Zeiss Axiophot equipment. For the microstructural analysis by SEM/EDS, Jeol JSM-6460 and Philips XL30 microscopes were used.

The XRD analysis was performed on powdered samples < 75 μm in a Panalytical X´PERT PRO diffractometer, using Cu Kα radiation (1.5418 Å), primary monochromator Kα1, with a voltage of 40 kV and 40 mA of current. The angular interval used was 20–70° 2θ, with a step of 0.020° and an acquisition time of 1.0 s per step.

For the chemical analysis, an *ad-hoc* methodology developed and described in a previously published paper by the authors [1] was adapted to the composition of AMC4. In Fig. 1, a diagram of the experimental procedure is shown. From the chemical composition data and information resulting from the mineralogical and microstructural analyses, the quantification of phases was performed by rational analysis [1] in a simple and accurate way.

A PANalytical, MagicX (PW-2424) spectrometer with an Rh anode X-ray tube (Super Sharp) and 2.4 kW generator was used, equipped with analytic software (IQ^+) for qualitative and semi-quantitative analysis based on the inter-elemental correction of fundamental parameters. The FRX technique was applied on powdered samples treated at 1200 °C to eliminate the resin and graphite and oxidize the aluminium and silicon. Pearls of the powder were prepared by melting with

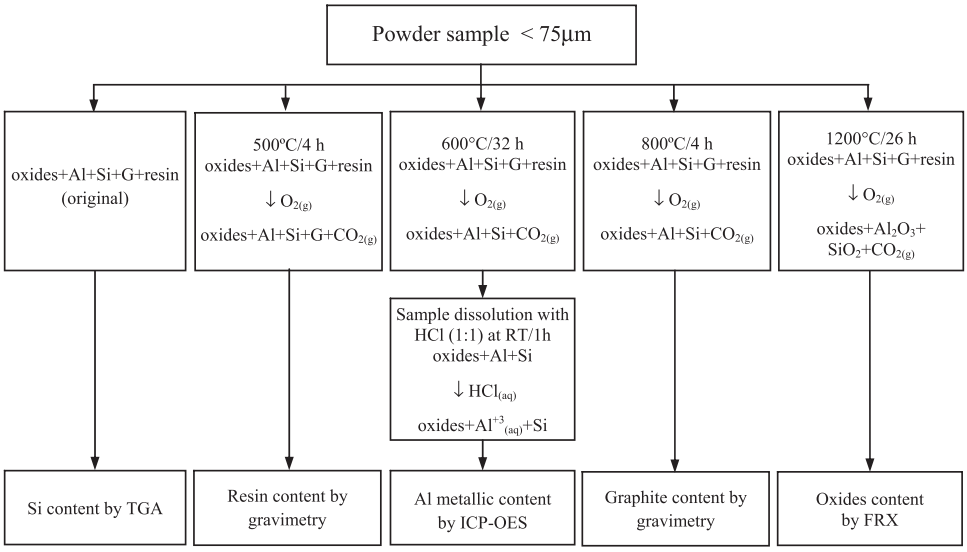

Fig. 1. Scheme of the methodology used for chemical analysis.

$Li_2B_4O_7$ at 1050 °C using a Perl'X3, Philips equipment and a Pt-Au crucible. The chemical analysis of these samples was performed employing calibration curves obtained from twenty-one (21) certified patterns of aluminosilicate materials, in the following ranges of concentrations for the majority elements: 0.16–88.8 wt% for Al_2O_3 and 0.96–43.5 wt% for MgO.

To quantify the metallic aluminium, an equipment Thermo Jarrell Ash IRIS Advantage Axial Inductively Coupled Plasma Optical Emission Spectrometer was used with a radiofrequency generator of 40.68 MHz and solid-state CIF (Charge Injection Device) detector. The Al was previously separated from a powdered sample (< 75 µm) treated at 600 °C (for resin and graphite elimination) by acid attack with HCl. Resin, and graphite contents were obtained by measuring the weight loss in the powdered samples after treatments at 500 and 800 °C, respectively, in order to selectively eliminate each of these components. A Sartorius BP 221 S9 analytical balance was used for this purpose. The quantification of silicon required a specific strategy, which is further described. Considering the resistance of this metal to dissolve in acids and alkalis, the content of Si was indirectly determined by thermogravimetry.

The granulometric characterization was performed by sieving powdered samples obtained from thermally treated fragments of the brick (~ 120 g) at 400 °C during 6 h in air. The aim of the heat treatment was to release particles via the pyrolysis of the organic binder.

The bulk density (ρ_b) and the apparent porosity (π_a) of AMC4 were determined in duplicate on cylinders 27 mm in diameter and 40 mm in height, based on the DIN 51056 standard [14]. A Sartorius BP 221S analytical balance and kerosene (as the fluid of known density) were used. The solid density (ρ_{pic}) was determined by helium pycnometry using a Quantachrome Multipycnometer and ~ 4.6 g of powder (< 210 µm). The true porosity (π_v) and the close porosity (π_c) were calculated using the following equations:

$$\pi v = \frac{(\rho pic - \rho b)x100}{\rho pic}$$

$$\pi_c = \pi_v - \pi_a$$

Mercury intrusion porosimetry was used to analyse the pore size distributions. This was done with a Micromeritics (USA) AutoPore II 9215 and fragments of bricks with a volume of ≈ 4.5 cm^3. To obtain the permeability of the refractory bricks, an in-house constructed device based on the ASTM C577 standard [15] was utilized. The technique uses a flow of gaseous nitrogen through a cubic specimen (5 cm in length) at a fixed differential pressure (240 mmHg).

The thermal differential and thermogravimetric analyses of AMC4 were carried out up to 1200 °C on powdered samples < 75 µm (13–19 mg) using Shimadzu DTA-50 and TGA-50 equipment respectively. Each run was performed with an air flow, Pt cells, alumina as a reference material and a heating rate of 10 °C/min. Static thermal treatments were also carried out between 400 and 1400 °C, in air, for 4 h using a heating rate of 10 °C/min. Irregular-shaped specimens of about 40 g and an electrical furnace with SiC heating elements were used. After the treatments, the fragments were ground and milled, and the mineralogical composition of the powders was determined by XRD using the same diffractometer and conditions employed in the analysis of the original brick powder.

To back up the analysis of thermal evolution, the equilibrium phases present in AMC4 between 700 and 1400 °C in an oxidant atmosphere (oxygen) was calculated using the commercial software FactSage V.7.1. The chemical composition of the refractories was used for the simulation, with the impurities not taken into account. Only the contribution of graphite to the C content was considered since the available databases do not have information regarding the resin or the residual carbon coming from its pyrolysis. To simulate the oxidant atmosphere, a system formed by 100 g of refractory and 3 g of gaseous O_2 was selected by taking a rough estimation of the amount of this gas in contact with the specimen in the furnace during the static thermal treatments. Furthermore, non-stoichiometric $MgAl_2O_4$ spinel was selected for the thermodynamic calculation.

For determining the permanent linear change (PLC) of AMC4, cylindrical samples (25 mm outer diameter and 50 mm in length) were successively subjected to three or five thermal cycles in air at 1000, 1200 and 1400 °C in duplicate. The treatments were done in an electrical furnace (SiC heating rates) with a heating rate of 10 °C/min up to the selected temperature. The specimens remained at this temperature for 2 h with free cooling afterwards. After each cycle, the length along the prism axis was determined. The permanent linear change was considered as the variation of the length with respect to the initial value (i.e., at the beginning of cycle 1). The global density and the apparent porosity of the treated specimens after each cycle were also determined by applying the same methodology used for the original materials.

The oxidation of the AMC4 refractory was evaluated by isothermal treatments of cylindrical specimens (25 mm in diameter and 2.5 cm in length), in an airtight environment (0.21 atm of O_2) at temperatures between 700 and 1400 °C, in duplicate. An electric chamber furnace with SiC heating elements was used, with the following heating schedule: heating rate of 10 °C/min from room temperature (RT) up to the

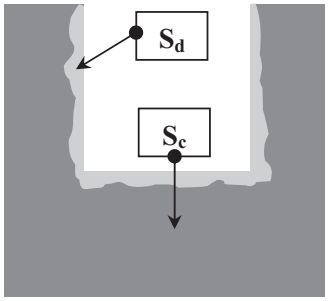

Fig. 2. Cross section of the corroded cup.

selected temperature, where it remained for 2 h, and free cooling afterwards. The treated cylinders were packed in polyester resin in a vacuum and cut crosswise.

The mass loss and the decarburized superficial area, both in percentages, were determined as gaseous corrosion indicators. Images of both cross surfaces of each sample were analysed using Image-Pro Plus v.6 software to estimate the decarburized area, which was considered as the peripheral region in which a reduction of the black or dark colour was visually detected. A radius delimiting the decarburized region from the central darker zone was defined, from which the decarburized area was calculated. The percentage of the total cross section corresponding to the decarburized area of the specimen was considered as the oxidation indicator.

The slag corrosion of AMC4 by a typical ladle slag (main components: 54.9 wt% CaO, 30.8 wt% Al_2O_3 wt%, 8.2 wt% MgO, 5.0 wt% SiO_2; basicity: 10.8 [16]) was studied at 1450 °C in air, employing the static cup test (cubes 5 cm in length, with a hole 3.6–3.7 cm in diameter and 2.3–2.5 cm in depth). The cup was thermally treated in an electric chamber furnace with SiC heating elements, at 1450 °C for 2 h. After the thermal treatments, the cup was packed in resin in a vacuum and cut transversally. Corrosion was measured by the worn cross-section of the cup, which was a consequence of the irreversible loss of the refractory particles attacked by the slag. Photos were taken of the cross sections and the images were analysed using Image-Pro Plus 6.0 software. The new inner surface of the cup was delimited in the cross section image and used to calculate the worn area S_d as a percentage of the original cross section of the cup, S_c (Fig. 2).

3. Results and discussion

3.1. Microstructural analysis

Optical and SEM/EDS images of AMC4 are shown in Figs. 3 and 4, respectively. Typical aggregates of brown fused alumina (EA) with large grains, low porosity and Ti-containing secondary phases were observed. Corundum grains also contain titanium and iron in solid solution, with percentages < 1 wt%. Between the alumina grains, the presence of phases with levels of SiO_2, Al_2O_3, and TiO_2 around 10–20 wt% as main components were detected by SEM/EDS. Moreover, two types of more porous and purer particles such as tabular alumina (TA and TA*) were identified as aggregates. From the microstructure and the presence of secondary phases with Al_2O_3, CaO and SiO_2 content higher than 8 wt%, one of these types of tabular alumina particles (TA*) is considered of poor quality and/or incompletely calcinated (see Fig. 3a).

From EDS mapping, it was inferred that MgO is mainly present as sintered coarse particles (> 100 μm), as can be seen in Fig. 4c for Mg mapping. These particles have secondary phases in their grain boundaries with a composition similar to C_2S (CaO/SiO_2 molar ratio < 2) and small amounts of Mg, Fe and Ti.

The microscopic analysis of the matrix by RLOM and SEM/EDS revealed the presence of graphite flakes, antioxidant metallic aluminium and silicon particles as well as fine particles of alumina. The graphite flakes have a purity higher than 96 wt%, with the typical minor components of the ashes, such as Al, Si, Mg and Fe. Meanwhile, the aluminium and silicon particles exhibited < 90 wt% purity, with small amounts of different solutes in each case (Fe, Ca, Mg, Ti, *etc*.).

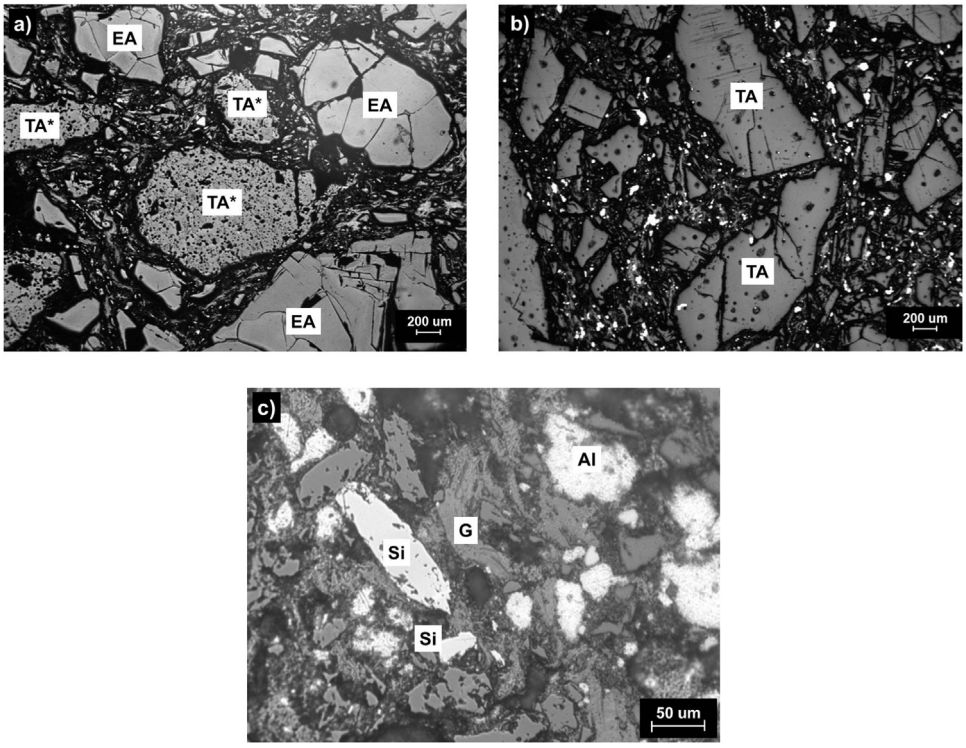

Fig. 3. Optical images of AMC4: aggregates (a and b) and matrix (c). (EA: brown fused alumina; TA: tabular alumina; TA*: low-quality tabular alumina; Si: silicon; Al: aluminium; G: graphite).

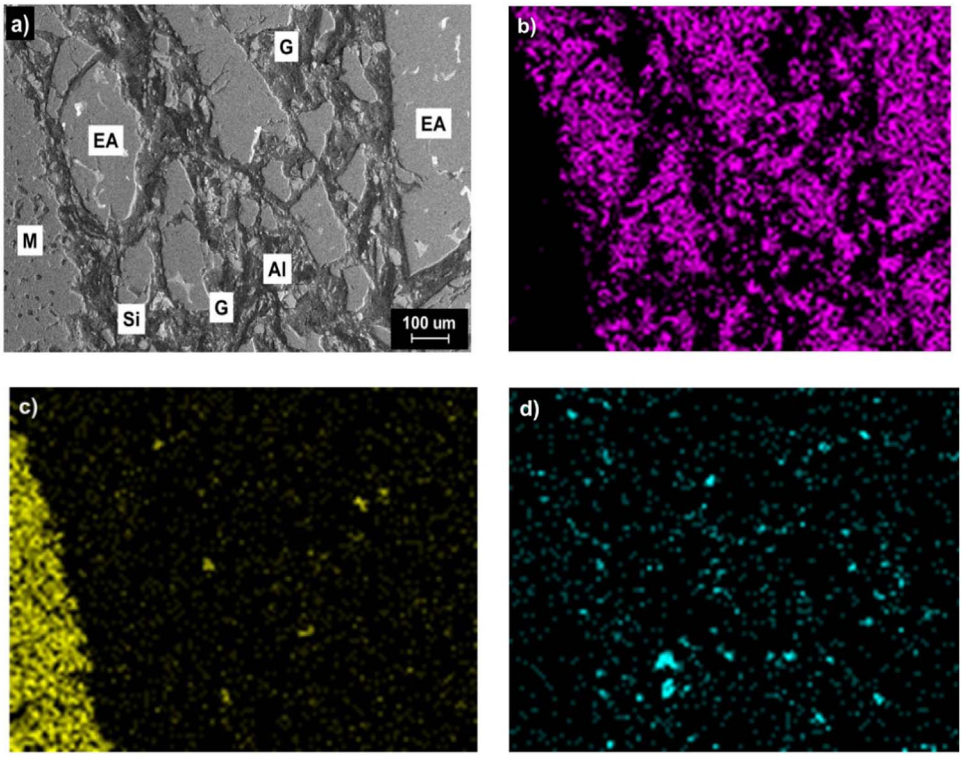

Fig. 4. SEM images of AMC4 (a) and Al (b), Mg (c) and Si (d) EDS mappings. (EA: brown fused alumina; M: magnesia; Si: silicon; Al: aluminium; G: graphite).

Graphite particles have a length, thickness and aspect ratio between 125-25 μm, 27-8 μm and 3.9–4.6, respectively, as a rough estimation. Moreover, most of the aluminium particles (~ 80%) have sizes between 10 and 50 μm, with a maximum size around 60 μm. The silicon particles are similar in size to those of Al.

3.2. Mineralogical analysis

The diffractogram of AMC4 is plotted in Fig. 5, from which the presence of the main crystalline phases observed by microscopic analyses was confirmed. The major phase is corundum (α-Al_2O_3; No. ICDD file: 00-011-0661), together with periclase (MgO; No. ICDD file: 00-045-0946) and graphite (C; No. ICDD file: 00-041-1487). Small peaks of metallic aluminium (Al; No. ICDD file: 00-004-0787) and silicon (Si; No. ICDD file: 00-027-1402) were identified as antioxidant additives. No other typical minor impurities in the raw materials, such as brucite ($Mg(OH)_2$), hematite (Fe_2O_3) or Ti-containing compounds could be detected by XRD.

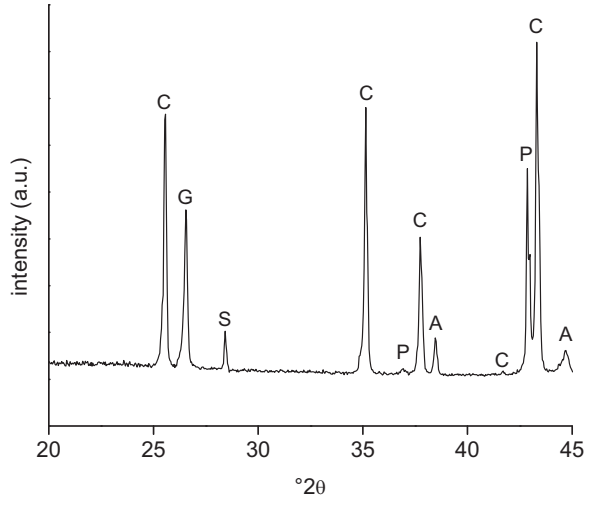

Fig. 5. Diffractogram of AMC4. (C: corundum, P: periclase, G: graphite, A: aluminium, S: silicon).

3.3. Granulometric analysis

Fig. 6 shows the particle size distribution of components for the AMC4 brick. This material has particles smaller than 4.76 mm (No. 4 mesh), with a percentage of fine (< 100 μm) and very fine (< 37 μm) particles of 14 wt% and 10 wt%, respectively. As can be observed in the plot of Fig. 6, there is a granulometric gap between 297 μm (No. 50 mesh) and 350 μm (No. 45 mesh); for this reason, statistical parameters D_{10}, D_{50} and D_{90} reported in Table 1 were calculated for both fractions, < 350 μm and > 350 μm.

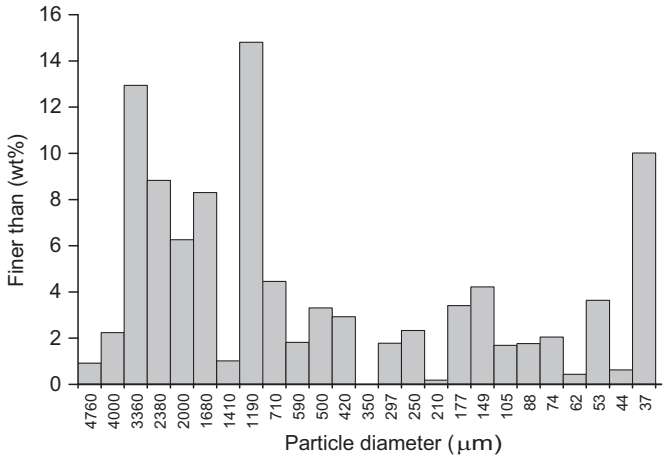

Fig. 6. Particle size distribution of AMC4.

Table 1
Statistical granulometric parameters of AMC4.

Fraction	Parameter	AMC4	AMC1	AMC3
> 350 μm	D_{10} (mm)	0.53	0.59	0.66
	D_{50} (mm)	1.59	1.60	2.13
	D_{90} (mm)	3.09	3.70	3.35
< 350 μm	D_{10} (μm)	< 37	< 37	< 37
	D_{50} (μm)	70	48	100
	D_{90} (μm)	226	230	239

The XRD patterns of samples of the following granulometric fractions (Fig. 7): < 65 μm, between 300 μm and 2 mm, and > 2 mm showed that magnesia is concentrated in the intermediate granulometric fraction. In the analysis, the relative intensities of peaks of periclase and corundum at 42.9 and 43.3°2θ, respectively, were compared. The proportion of MgO in the fine fraction (< 66 μm) ended up being very small, even less than in the coarse aggregates fraction (> 2 mm), as was anticipated in the microstructural analysis by SEM/EDS.

3.4. Textural analysis

Density and porosity values of AMC4 are given in Table 2. The picnometric density (ρ_{pic}) is in agreement with the densities of the main components of the refractory (tabular alumina ~ 3.9 g/cm^3; brown fused alumina ~ 3.92–3.94 g/cm^3, sintered magnesia ~ 3.4 g/cm^3, graphite ~ 2.2 g/cm^3, resin ~ 1.2 g/cm^3, aluminium: 2.7 g/cm^3, silicon: 2.3 g/cm^3). Moreover, AMC4 has similar amounts of open (π_a) and closed (π_c) pores in its structure.

The pore size distribution of AMC4 is plotted in Fig. 8, showing the two typical populations present in this type of material: pores larger than 100 μm which correspond to packing defects, and pores < 100 μm located between fine particles in the matrix and inside particles. Table 3 shows the contribution of different pore sizes (D) in the range of small pores (< 10 μm), where the ranges of pores playing an important role in the resistance to fluid penetration (< 1 μm [13] and < 5 μm [17]) are included.

Regarding the permeability of AMC4, it falls below the minimum value measurable by the equipment used. It can only be asserted that the permeability value is lower than 0.3 mD.

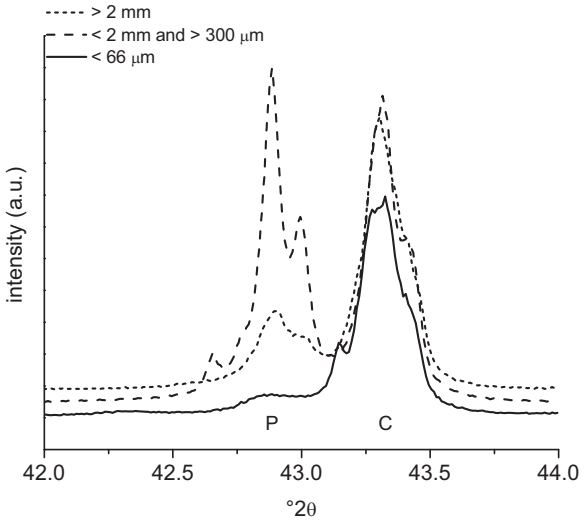

Fig. 7. Diffractograms of different granulometric fractions of AMC4 particles. (C: corundum; P: periclase).

Table 2
Density and porosity values.

	ρ_b (g/cm^3)	ρ_{pic} (g/cm^3)	π_a (%)	π_c (%)	π_v (%)
AMC4	3.33 ± 0.02	3.58 ± 0.03	3.6 ± 0.1	3 ± 1	7 ± 1
AMC1	3.45 ± 0.02	3.14 ± 0.02	6.7 ± 0.1	2 ± 2	9 ± 2
AMC3	3.39 ± 0.02	3.14 ± 0.01	4.0 ± 0.1	3 ± 2	7 ± 2

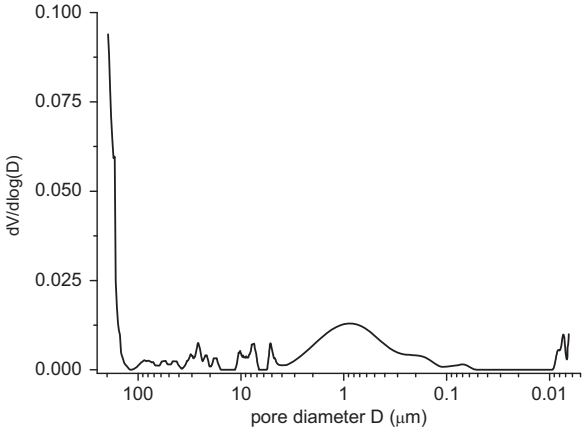

Fig. 8. Pore size distribution of AMC4.

Table 3
Pore size distributions for small pores (< 10 μm).

Materials	Volume percentage (%)		
	10 μm < D < 5 μm	5 μm < D < 1 μm	1 μm < D
AMC4	44.2	42.7	13.0
AMC1	63.1	34.6	2.3
AMC3	60.9	34.9	4.2

3.5. Thermal analysis

DTA and TGA thermograms of AMC4 up to 1200 °C are shown in Fig. 9. The main DTA peaks are marked in the corresponding plot. Meanwhile only two mass losses are clearly observed in the TGA thermogram. Exothermic peaks between 200 and 500 °C are attributed to the pyrolysis of resin, which is accompanied by a mass loss (TGA) of 2.3 wt% due to volatile elimination. At higher temperature, a small endothermic peak around 660 °C produced by the melting of aluminium is observed in DTA thermogram. At ~ 750 °C, an intense exothermic peak denotes the direct oxidation of carbon ($C_{(s)} + 1/2\ O_{2(g)} \rightarrow CO_{2(g)}$), with an associated mass loss of 3.8 wt%. Whether the oxidation of the

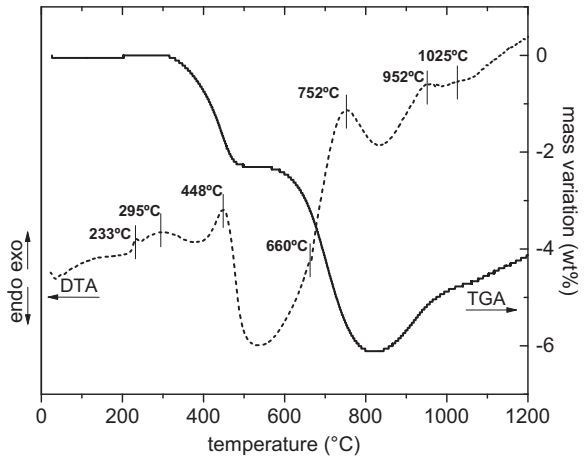

Fig. 9. DTA/TGA thermograms of AMC4.

Table 4
Reactions between AMC4 components.

Reaction	$\Delta G_R^{1000\,^\circ C}$ (Kcal)	Δm (wt%)	ΔV (%)
(1) $2\,Al_{(s)} + 1.5\,O_{2(g)} \rightarrow Al_2O_{3(s)}$	− 303.60	+ 89	+ 166
(2) $Si_{(s)} + O_{2(g)} \rightarrow SiO_{2(s)}$	− 163.28	+ 114	+ 146
(3) $4\,Al_{(l)} + 3\,C_{(s)} \rightarrow Al_4C_{3(s)}$	− 32.13	0	+9
(4) $MgO_{(s)} + 2\,Al_{(l)} + 3\,CO_{(g)} \rightarrow MgAl_2O_{4(s)} + 3C_{(s)}$	− 146.33	+ 89	+ 105
(5) $MgO_{(s)} + 2\,Al_{(l)} + 1.5\,O_2 \rightarrow MgAl_2O_{4(s)}$	− 307.09	+ 51	+ 78
(6) $4\,MgO_{(s)} + 2\,Al_{(l)} \rightarrow MgAl_2O_{4(s)} + 3\,Mg_{(g)}$	+ 30.29	− 34	− 29
(7) $MgO_{(s)} + Al_2O_{3(s)} \rightarrow MgAl_2O_{4(s)}$	− 3.43	0	+8
(8) $2\,Si_{(s)} + CO_{(g)} \rightarrow SiO_{(g)} + SiC_{(s)}$	− 10.86	− 29	− 49
(9) $Al_4C_{3(s)} + 8\,MgO_{(s)} \rightarrow 2\,MgAl_2O_{4(s)} + 3\,C_{(s)} + 6\,Mg_{(g)}$	+ 92.73	− 30	− 36
(10) $Al_4C_{3(s)} + 2\,MgO_{(s)} + 6\,CO_{(g)} \rightarrow 2\,MgAl_2O_{4(s)} + 9\,C_{(s)}$	− 260.50	+ 75	+ 50
(11) $Al_4C_{3(s)} + 2\,MgO_{(s)} + 3\,O_{2\,(g)} \rightarrow 2\,MgAl_2O_{4(s)} + 3\,C_{(s)}$	− 582.03	+ 43	+ 10
(12) $3\,Al_2O_{3(s)} + 2\,SiO_{2(s)} \rightarrow 3Al_2O_3.2SiO_{2(s)}$	− 3.67	0	+ 10
(13) $SiC_{(s)} + 2\,MgO_{(s)} + 2\,CO_{(g)} \rightarrow Mg_2SiO_{4(s)} + 3\,C_{(s)}$	− 56.00	+ 46	+ 70
(14) $SiC_{(s)} + 2\,MgO_{(s)} + 1.5\,O_{2(g)} \rightarrow Mg_2SiO_{4(s)} + CO_{(g)}$	− 216.70	+ 17	+ 3

glassy-carbon coming from resin is included in the first or the second mass loss along with graphite cannot be inferred just from these data alone.

Moreover, peaks with low definition and intensities were observed at temperatures > 900 °C; in a DTA scan up to 1400 °C under similar conditions, no well-defined peaks were observed at temperatures higher than 1200 °C either. These small peaks were attributed to reactions involving the metallic additives (Al and Si) themselves or the product of their interactions, such as those reactions indicated in Table 4 [2,5,6,9,18]; the temperature from which each reaction takes place increased from the first reactions (900–1000 °C) to the latter (around 1300 °C). Reaction of Al with residual carbon or graphite to form the metallic carbide (reaction (3)), as well as the related reactions (9)–(11), hardly took place due to the oxidant nature of the atmosphere.

Several of the reactions of Table 4 are accompanied by changes in mass (Δm). In fact, a continuous increase of mass is displayed in the TGA curve from 840 °C, which slows down when the temperature reaches ~ 1000 °C. At 1200 and 1400 °C, the mass increased in 2.1 wt% and 2.6 wt%, respectively.

Table 5 shows the crystalline phases identified in XRD patterns of powdered samples of brick fragments treated at different temperatures between 400 and 1400 °C in air.

After treatment at 400 °C, the reactions occurring in AMC4 did not appear in the diffraction pattern, as they relate to the first steps of resin pyrolysis. Thus, no significant changes were observed up to 700 °C, when the amount of graphite notably reduced. None of its diffraction peaks was detected at 1000 °C onwards.

On the other hand, the amount of aluminium strongly decreased after treatment at 1000 °C due to the reaction with carbon (probably the more reactive glassy-C) to form Al_4C_3 (reaction (3) of Table 4), prior to melting at 660 °C, according to the presence of very small peaks corresponding to this phase (No. ICDD file 00-001-0953) in a diffractogram obtained with a smaller step and with a longer acquisition time (no peaks of Al_4C_3 were identified when the diffractogram was obtained in the current conditions). Moreover, Al (and also the carbide) can react with magnesia to form $MgAl_2O_4$ spinel (see reactions of Table 4); according to what was derived from the XRD analysis, the first indications of the presence of spinel appeared around 1000 °C, when aluminium peaks completely disappeared. The intensity of main peaks of periclase seems to decrease just at 1100 °C. The content of magnesia clearly diminished at higher temperatures, and as a consequence, the intensity of MA spinel peaks increased. At 1400 °C, periclase was still present in AMC4.

Regarding the transformation of Si, the intensity of the main diffraction peaks decreased after treatment at 1000 °C and finally disappeared when the treatment temperature reached 1400 °C. However, no other crystalline phase coming from other reactions involving silicon (see reactions of Table 4), was identified; none of these phases was identified in a sample treated at 1400 °C in a graphite bed either. In order to get more information about these phases, a treatment at 1400 °C was performed on a powdered sample of a granulometric fraction < 62 μm (this fraction was obtained similarly to the sample for granulometric analysis). In the X-ray diffractogram of the treated powder, only small peaks of mullite ($3Al_2O_3.2SiO_2$; No. ICDD file: 00-001-0613) were detected (reaction (12), Table 4). The presence of titanium oxides, such as rutile (TiO_2; No. ICDD file: 00-021-1276) and Ti_3O_5 (No. ICDD file: 01-072-2101), were also identified in samples treated at 1400 °C. These minor phases come from the titanium impurities of brown fused alumina particles, typical of this raw material (as was detected by SEM/EDS), and they are responsible for the blue colour observed in particles of samples treated at this temperature.

3.6. Chemical analysis

From DTA/TGA data, temperatures for thermal treatments conducive to oxidizing specific refractory components were defined. Then, thermally treated powders were analysed by FRX, ICP-OES and gravimetric techniques according to the scheme shown in Fig. 1.

TGA thermograms of materials treated at 500 and 800 °C/4 h and the corresponding diffractograms in the region of °2θ where graphite

Table 5
Phases identified by XRD in AMC4 specimens treated at various temperatures (the amount of + is an indicator of the proportion of each phase; the number of the IDCC file is indicated in parentheses).

	Corundum (11-0661)	Periclase (45-0946)	Graphite (41-1487)	Al (4-0787)	Si (27-1402)	Spinel (45-0946)	Others
Original	+ + + +	+ +	+ +	+	+	n.d.	n.d.
400 °C	+ + + +	+ +	+ +	+	+	n.d.	n.d.
700 °C	+ + + +	+ +	+	+	+	n.d.	n.d.
1000 °C	+ + + +	+ +	n.d.	n.d.	+	+	Al_4C_3
1100 °C	+ + + +	+ +	n.d.	n.d.	+	+	n.d.
1200 °C	+ + + +	+	n.d.	n.d.	+	+ +	n.d.
1400 °C	+ + + +	+	n.d.	n.d.	n.d.	+ +	TiO_2, Ti_3O_5 mullite

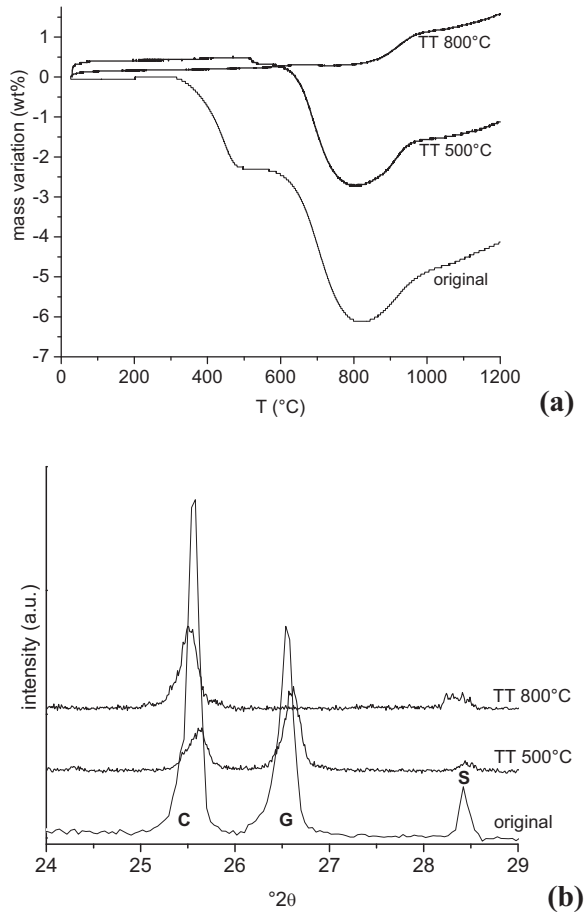

Fig. 10. Thermograms (a) and diffractograms (b) of original and thermally treated samples (TT) of AMC4 (500 and 800 °C/4 h).

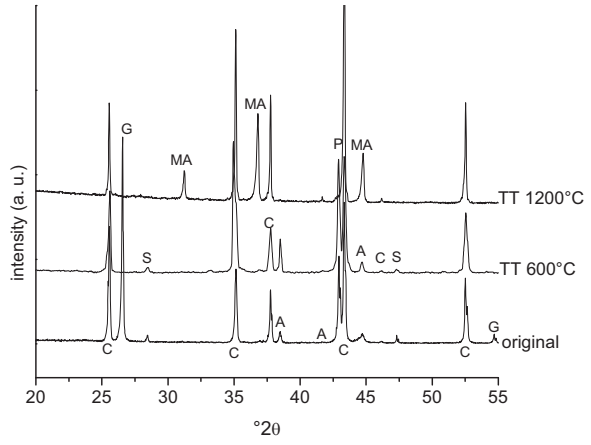

Fig. 11. Diffractograms of the original and thermally treated samples (TT) of AMC4 at 600 °C/32 h and 1200 °C/26 h. (C: corundum; P: periclase; G: graphite; A: aluminium; S: silicon; MA: $MgAl_2O_4$ spinel).

has the most intense peak (26.38°2θ; No. ICDD file 00-041-1487) are shown in Fig. 10. The mass loss at temperatures < 700 °C linked to the pyrolysis of resin is not displayed in the TGA curve of the powder treated at 500 °C, although the step around 800 °C due to the elimination of carbon by direct oxidation persists. The presence of graphite is verified in the sample treated at 500 °C (Fig. 10a). Conversely, no mass loss is displayed of TGA in the sample after treatment at 800 °C and consistently, the most intense peak of graphite was not identified in the corresponding XRD pattern (Fig. 10b). These observations confirm the effectiveness of eliminating resin and graphite separately in each thermal treatment.

Diffractograms of powders treated at 600 °C/32 h and 1200 °C/26 h are shown in Fig. 11. The disappearance of the most intense peak of graphite (26.38°2θ; No. ICDD file: 00-041-1487) and the persistence of peaks of aluminium (38.47°2θ; No. ICDD file: 00-004-0787) and silicon (28.44°2θ; No. ICDD file 00-027-1402) was confirmed in the diffractogram of the sample treated at 600 °C for 32 h. Conversely, after treatment at 1200 °C, main peaks of Al, Si and periclase (No. ICDD file: 00-045-0946) were not identified; in agreement, $MgAl_2O_4$ spinel (No. ICDD: 00-021-1152) was detected in this sample.

As mentioned above, silicon is difficult to dissolve in a liquid medium in order to measure its content with a method similar to that used for Al. Taking into account the XRD results for the sample thermally treated at 1200 °C for 26 h (Fig. 11) where no peaks of Al and Si were identified, it was assumed that the mass increase exhibited for TGA in the AMC4 powdered sample between 800 °C and 1200 °C in air (see Fig. 9) was mainly a consequence of the oxidation of Al and Si, corresponding to reactions (1) and (2) of Table 4 (according to thermal evolution analysis, the formation of a small amount of spinel could also occur). Thus, the amount of silicon was estimated by measuring the difference from the mass increase in TGA at 1200 °C once the aluminium content was obtained by ICP-OES.

The chemical composition of the AMC4 refractory is given in Table 6. Aluminium and silicon content was confirmed by XRD analysis using the Rietveld refining method for quantification purposes: 2.5 wt% of Al and 0.17 wt% of Si. The smaller amount of silicon determined by XRD could be a consequence of the orientation of graphite and periclase particles (in spite of the cares to avoid the orientation in the sample) and/or the occurrence of another process such as spinel formation overlapped with the oxidation of Al and Si, producing an overestimation of the Si proportion from the TGA data. The titanium content was higher in comparison with the amount of this impurity in the previously characterised AMC bricks [1,2]. This could be the reason for the clear detection of Ti oxides in the AMC4 treated at 1400 °C (Section 3.5).

The content of resin, calculated by the mass loss after thermal treatment at 500 °C, was 4.4 wt% (Table 6). On the other hand, the graphite percentage was estimated as the difference between the mass loss after treatment at 800 °C (6.3 wt%) and at 500 °C, giving 1.9 wt% (Table 6). Bearing in mind these results, it was concluded that the first step in the TGA curve (Fig. 9) is just due to the elimination of resin volatiles but does not include the loss of material by residual carbon oxidation. Then, the amount of volatiles of the organic binder is estimated at 2.3 wt%. Buchebner et al. [19] have reported that 45 wt% of the phenolic resin is converted into residual carbon; in consequence,

Table 6
Chemical composition of AMC4.

Weight percentage (wt%)									
Al_2O_3	Al	Fe_2O_3	MgO	SiO_2	Si	CaO	TiO_2	Resin	Graphite
77.7 ± 0.5	2.8 ± 0.1	1.80 ± 0.05	6.6 ± 0.1	2.67 ± 0.05	0.35 ± 0.05	0.30 ± 0.05	1.48 ± 0.04	4.4 ± 0.1	1.9 ± 0.1

Table 7
Solid phases in equilibrium in AMC4 at temperatures between 700 and 1400 °C.

T	Weight percentage (wt%)								
	Al_2O_3	Al	MgO	Spinel[a]	Sapphirine[b]	Graphite	Si	SiC	Mullite
RT	87.00	3.15	7.40	–	–	2.15	0.39	–	–
700 °C	71.65	–	–	23.67	2.37	2.01	–	0.29	–
1000 °C	71.47	–	–	23.85	2.37	2.01	–	0.29	–
1100 °C	71.13	–	–	24.19	2.37	2.01	–	0.29	–
1200 °C	70.38	–	–	24.95	2.37	2.01	–	0.29	–
1400 °C	65.32	–	–	31.10	–	2.01	–	0.29	1.28

[a] From 78.76 wt% (700 °C) to 47.1 wt% (1400 °C) of $MgAl_2O_4$.
[b] $Mg_4Al_{10}Si_2O_{23}$.

the remaining 55 wt% p/p corresponds to volatile species. Taking into account this information, the amount of resin and glassy carbon calculated from the TGA data are 4.2 wt% p/p and 1.9% p/p (0.45 × 4.2), respectively. On the other hand, the second step in the thermogram (3.8 wt%) should correspond to the elimination of graphite and residual C, from which the amount of graphite can be estimated to be 1.9 wt% p/p. Thus, the content of resin and graphite estimated from the TGA are in agreement with those values determined by gravimetry.

Bearing in mind the considerations for the rational analysis applied to other AMC refractories [1], it can be concluded that the proportion of phases present in AMC4 are approximately: 77.7 wt% of corundum, 6.6 wt% of periclase, 4.4 wt. of phenolic resin, 2.8 wt% of Al, 0.3 wt% of Si, 1.9 wt% of graphite and 6.3 wt% of impurities. These minor components include Fe_2O_3, SiO_2, CaO and TiO_2 and come from the typical secondary phases accompanying the corundum, periclase and graphite particles [1], which were also detected by SEM/EDS.

The chemical composition of AMC4 (dismissing impurities and organic binder) was used to calculate the composition of the system at equilibrium between 700 and 1400 °C in an oxidant atmosphere. The percentages of solid phases in this temperature range are reported in Table 7.

According to the thermodynamic simulation, significant transformation occurs in AMC4 at 700 °C, but the mineralogical composition at equilibrium does not change much at higher temperatures. From 700 °C onwards, MgO and Al convert completely into spinel, and the ternary oxide sapphirine ($Mg_4Al_5Si_2O_{23}$, $M_4A_5S_2$). 'Spinel' phase is constituted mainly, but not only, of $MgAl_2O_4$ (MA); other structures related to the non-stoichiometric character of this solid are also part of spinel. This is the reason why being the only Mg-containing phase, the percentage of spinel at 1400 °C is higher than the amount which can be formed if all of MgO reacts (~ 26 wt%): Al_2O_3 is likely dissolving in the spinel structure, which is why the proportion of this phase tends to grow as temperature increases.

It is worthy to note that the amount of graphite decreases at 700 °C, but then it remains constant up to 1400 °C, retaining 93% of the original amount. On the other hand, silicon reacts with carbon to form SiC and just at 1400 °C mullite is in an equilibrium solid phase, and as a consequence, there is a greater decrease in the content of alumina.

Comparing the equilibrium composition with the results of the thermal evolution of AMC4 between 700 and 1400 °C (Section 3.5), the thermodynamic simulation provides a good description of the main phases formed, with differences in the amount and the thermal stability field of each phase. This is mainly a consequence of the textural and granulometric effects, dismissed in the thermodynamic simulation. Moreover, the amount of oxygen used for the simulation could be not enough to reproduce the actual oxidant atmosphere. The equilibrium phases which were not identified by XRD in the thermally treated samples of AMC4 were SiC and $M_4A_5S_2$. It cannot be ruled out that the quantity of these phases formed in the treated samples were smaller than the limit detection of the XRD technique. Nevertheless, it is difficult for a ternary compound in a real system to form at intermediate temperatures (between 700 and 1200 °C) because of diffusion restrictions.

On the other hand, Al_4C_3 was not predicted as an equilibrium phase despite the fact that it was identified by XRD after treatment at 1000 °C. However, a simulation under less oxidant conditions (i.e., without the addition of 3 g of O_2), anticipate the formation of aluminium carbide between 700 and 1400 °C. The appearance of Al_4C_3 in the thermally treated AMC4 specimens could indicate that the oxygen partial pressure in the environment of the Al particles was quite lower than that imposed by the external atmosphere.

3.7. Permanent linear change (PLC)

The permanent linear change (PLC) after treatment at three different temperatures, 1000, 1200 and 1400 °C, are plotted against the number of cycles in Fig. 12a. The variations in the bulk density and apparent porosity after each cycle are shown in Fig. 13.

When PLC was determined after cycling at 1200 °C, a slight tendency to increase with the number of cycles was observed (Fig. 12a), although the variations in bulk density and apparent porosity were similar to those measured after treatments at 1000 °C (Fig. 13). This behaviour is due to the presence of $MgAl_2O_4$ spinel (identified in AMC4 from 1000 °C), which is known to be the main cause for the residual expansion of this type of refractories. The effect of the spinel formation on the refractory structure depends on which of the several mechanisms is the most dominant (see reactions of Table 4), but in general it produces residual expansion. Furthermore, spinel formation leads to a reduction in the solid density and can also generate additional porosity and fissures [18,20–22].

At 1400 °C, there is significant residual expansion which increases continuously up to the last cycle reaching a PLC of 1.3%. The changes in bulk density and the volume fraction of open pores follow the same tendencies exhibited at lower temperatures. However, the porosity increased slowly as a function of cycling, which is partially attributed to the sintering of fine particles. Conversely, the value of ρ_b after treatments at 1400 °C falls to lower values for the same number of cycles than those after 1000 and 1200 °C. This is an indicator of the further advance of spinel formation, which was confirmed by XRD.

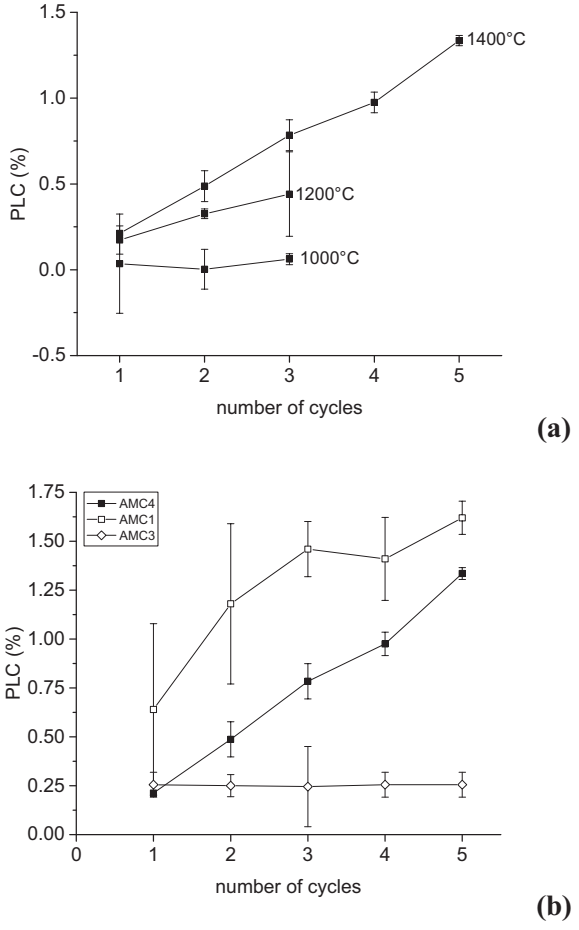

Fig. 12. Permanent linear change in function of the number of cycles: (a) AMC4 at different temperatures and (b) AMC4, AMC1 and AMC3 at 1400 °C.

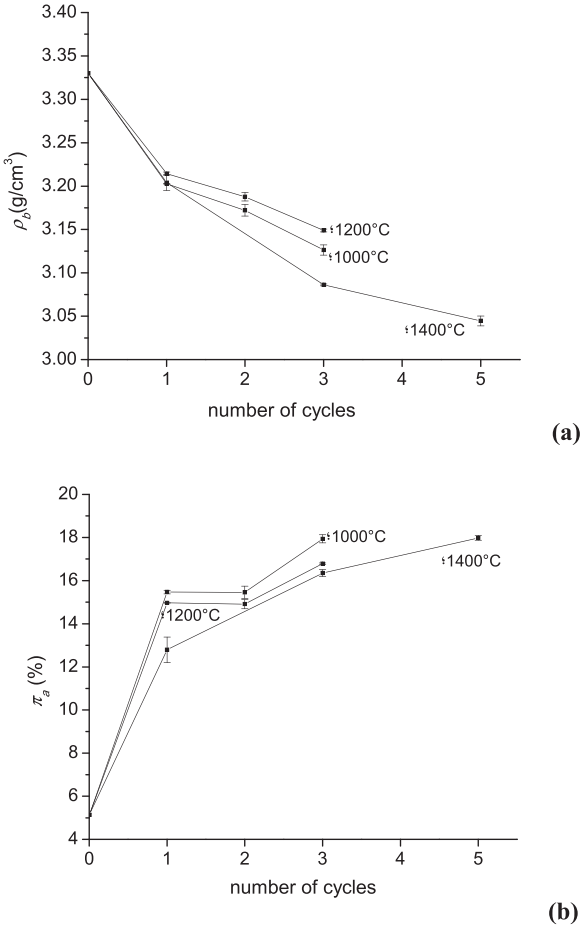

Fig. 13. Variation in bulk density (a) and apparent porosity (b) during PLC testing of AMC4.

3.8. Oxidation resistance

Images of the cross surfaces of specimens treated in air in the range 700–1400 °C are shown in Fig. 14, together with an image of the original AMC4 brick. Percentages of the decarburized area and mass loss as the treatment temperature increases are plotted in Fig. 15.

From 300 °C onwards, the main processes involving mass loss are the pyrolysis of resin and the direct oxidation of graphite, which also produces discolouring of samples. Resin pyrolysis as a thermally activated process will take place throughout the entire specimen. However, the catalytic effect of O_2 [23,24] will produce a gradient in the advance of the transformation as the gas penetrates the material. Meanwhile, direct oxidation of graphite will occur mainly in the outer layers in contact with oxygen and spread towards the interior of the specimen as the O_2 of air enters through the open pores, giving the typical patterns observed in most of the cross surfaces of Fig. 14.

After treatment at 700 °C, no decarburized zone was observed in AMC4 specimens (Fig. 14). In tune with this, a weight loss (~ 4.3 wt%) equivalent to the amount of resin was determined, indicating that the pyrolysis was complete (including the oxidation of the glassy-carbon), but the direct oxidation of graphite was not significant after 2 h at 700 °C.

When the oxidation test was performed at 1000 °C, a notable external decarburized area was detected in the cross surfaces (but not complete, not even in the outer peripheral area) suggesting that graphite loss took place in this condition. However, only a small increase in mass loss was determined. The reason for this disagreement is that processes involving mass increases, such as the oxidation of silicon for instance (Section 3.3), overlapped the graphite loss.

At higher temperatures, 1200 and 1400 °C, the percentage of decarburized area did not show a significant change, but a higher decarburization of the entire cross surface is evident, being more pronounced at the highest temperature, especially in the outer layer. Moreover, mass loss decreased with respect to that determined after treatment at 1000 °C, which indicates advances in those processes associated with positive mass variation (see reactions of Table 4).

The constancy of the decarburized area was observed in other AMC materials, and reasons for this behaviour have already been discussed [16]. The advance of direct graphite oxidation, responsible for the discolouration, depends on the interplay between several factors [16] that determine oxygen diffusion into the specimen: the porosity of the decarburized layer and the difference of the oxygen concentration between the external atmosphere and specimen's interior. As can be inferred from Fig. 11b, the volume fraction of open pores decreases from 1000 to 1400 °C, which can be one of the reasons for the lack of significant change in the radial advance of the decarburization front. For instance, the formation of soot as a sub-product (formed by: 2 CO → CO_2 + $C_{(s)}$) [25], could block pores that contribute to reducing the

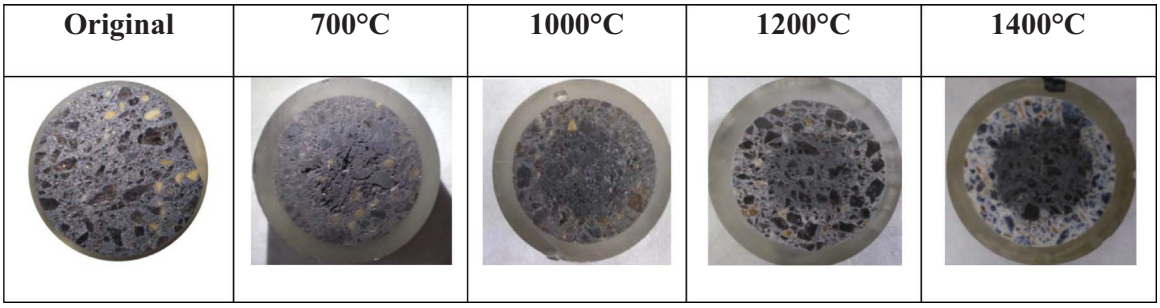

Fig. 14. Cross surface images of AMC4: original and thermally treated in air.

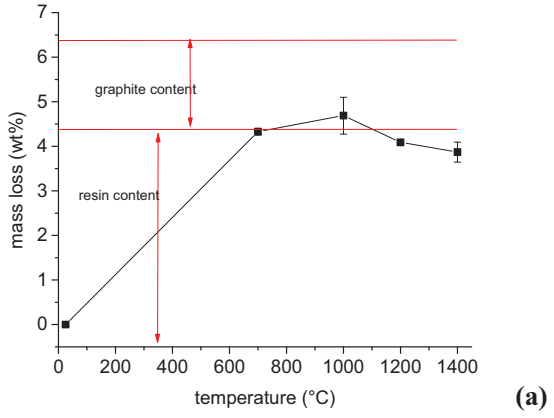

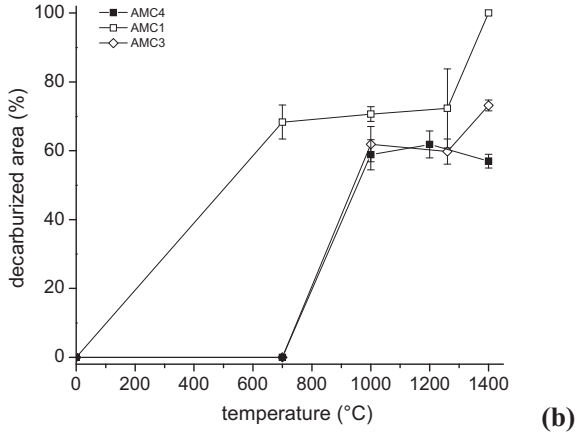

Fig. 15. Percentage of mass loss (a) and decarburized area (b) of AMC refractories as a function of the treatment temperature (the lines only join the media values for clarity).

porosity and the mass loss. On the other hand, the counter-diffusion of the gaseous reaction products could partially inhibit entrance of O_2 gas.

3.9. Slag corrosion resistance

Fig. 16 shows an image of the cross surface of the tested cup, carried out at 1450 °C. As can be observed, superficial decarburization occurred during the corrosion test. The wear produced by the molten slag attack was estimated at 5%.

3.10. Comparison with other AMC refractories

For the comparison between the characteristics and chemical properties of AMC4, AMC1 and AMC3 bricks, previous data reported for the last two materials [2] are used.

AMC1 and AMC3 are similar in composition to AMC4. The main differences are the amount of Al, which is greater in AMC4, and the

Fig. 16. Cross section of the corroded cup of AMC4 (1450 °C) (black line: original cup inner surface; white line: cup inner surface after slag corrosion).

presence of metallic silicon as an antioxidant additive. On the other hand, in the three refractories, tabular and fused alumina are used as raw materials; AMC3 is the only refractory containing bauxite, and the quality of tabular alumina seems to be poor in AMC4. In spite of the similarities in the content and type of magnesia (sintered grains), this component is coarser in AMC4. Magnesia particles are part of the fine granulometric fraction (< 120 μm) in AMC1 and AMC3, contrary to the distribution of this component in AMC4, where these particles are coarser (Section 3.3). As for graphite flakes, the particles present in AMC4 are globally shorter and with smaller aspect ratio than those composing AMC1 and AMC3.

The accumulative curves of particle size distribution for the three materials altogether (obtained with the same procedure as that depicted for AMC4) are shown in Fig. 17. Similar to that observed for AMC4, there is a granulometric cut at 350 μm. The statistical parameters of each population of particle sizes, larger and smaller than 350 μm, are reported in Table 1 for AMC1 and AMC3.

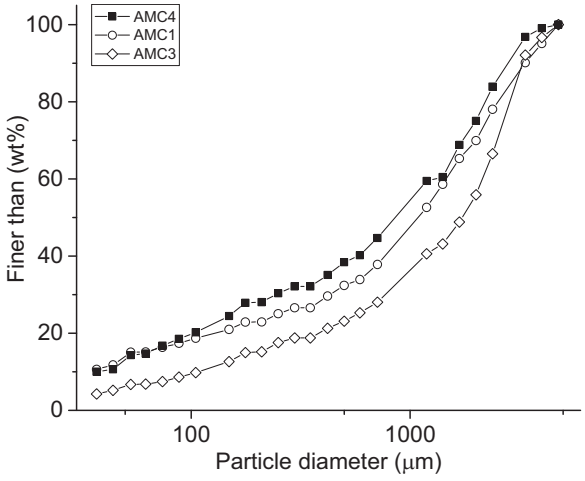

Fig. 17. Cumulative particle size distribution of the three AMC refractories.

According to the accumulative curves and statistical parameters, AMC4 and AMC1 have similar particle size distributions, although the granulometric fraction > 350 μm of AMC1 is slightly finer and wider than that of AMC4. On the other hand, AMC3 has coarser particles throughout the whole range of determined sizes, with a lower percentage of particles smaller than 37 μm (around 4 wt% with respect to ~ 10 wt% for the other two refractories).

Regarding the bricks' texture, porosity values of AMC1 and AMC3 are reported in Table 2. The amount of porosity, considering close as well as open pores, is very similar between AMC4 and AMC3, whereas AMC1 exhibited higher apparent and total porosities. The whole range of pore sizes was similar for the three types of AMC refractories, with differences in the distribution along this range. The most interesting pore sizes are those smaller than 10 μm, because they are the interparticle voids which play an important role in the resistance to fluid penetration. According to that reported by Kashcheev and Semyannikov [17], a molten steelmaking fluid does not penetrate pores smaller than 5 μm in the refractory structures. The contribution of this pore size range in the whole range is quite larger in AMC4 (~ 85%) than in AMC1 (~ 30%) and AMC3 (~ 20%). Moreover, the volume of pores < 1 μm has been associated with the permeability of similar refractories [12]. Considering the data of Table 3, AMC4 has a greater amount of pores < 5 μm and < 1 μm, than the other two materials, which exhibited similar pore size distributions with the exception of the amount of pores finer than 1 μm (AMC3 has almost twice the volume percentage of AMC1). The presence of fine particles of silicon in AMC4 could be the reason for its finer pore distribution.

With regard to permeability, AMC1 and AMC3 were characterised by using equipment different from that used for AMC4, as was previously reported [1,2], giving the following values for a differential pressure (ΔP) of 3 bar: 0.130 and 0.009 cm^3/dyn/s. This difference was attributed to the smaller apparent porosity and pore sizes of AMC3. As was mentioned before, the pores which differentiate AMC1 from AMC3 are those smaller than 1 μm. Furthermore, AMC3 has a small population of pores in the fraction smaller than 0.01 μm, which better resists the gas flow, and which is absent in AMC1; the minimum pore size determined in AMC1 and AMC3 was ~ 0.05 and ~ 0.008 μm, respectively. This porosity characteristic is now considered the main reason for the remarkable difference between the permeability of these two materials.

In order to obtain a better approximation of the permeability of AMC4, an estimation can be done considering the pore size distribution of this material in comparison with that of AMC1 and AMC3. As was mentioned above, AMC4 has smaller pores than AMC1 and AMC3 bricks. Moreover, AMC4 has open pores finer than 0.01 μm like AMC3, but the volume fraction of this size range of pores is larger. The minimum pore size of AMC4 is also smaller than that of AMC3, around 0.005 μm. Bearing all these characteristics of open porosity of AMC4 in mind, and considering its slightly lower apparent porosity, it was concluded that AMC4 surely has less permeability than AMC3.

The differences in the characteristics of the three AMC refractories analysed here have an impact on their properties, such as PLC and chemical resistance. In Fig. 12b, the PLC values are shown for AMC4, AMC1 and AMC3 in function of the number of cycles after treatment at 1400 °C. As can be observed in the diffractograms after the first cycle at this temperature, shown in Fig. 18, the advance of MA spinel formation was higher in AMC1 (higher intensity of MA peaks and a lower intensity of the main periclase peak), which was attributed to the small size of particles, especially those of magnesia.

This is the main reason why the PLC of this material is always greater than that of AMC4. In this material, spinel formed slowly and continuously increased with the number of cycles, contrary to the behaviour of AMC1; in the latter, the PLC was not significant after the first cycle, because the amount of MA was almost the maximum (21 wt%) after this cycle [2]. AMC3, with a similar MgO content as AMC1 also concentrated in the same medium-fine fraction exhibited a remarkably small PLC, which has been previously discussed in a paper published by the authors [2].

As for the resistance to oxidation by air, AMC4 showed behaviour similar

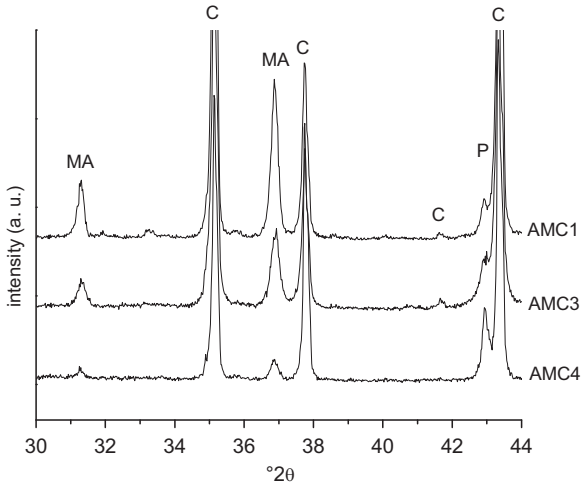

Fig. 18. Diffractograms of the three AMC bricks after one cycle at 1400 °C in PLC testing. (C: corundum, P: periclase, MA: $MgAl_2O_4$ spinel).

to that of AMC3, as can be inferred from plot of Fig. 15b, except during treatment at 1400 °C, when AMC4 performs better. On the other hand, both AMC refractories exhibited a higher resistance to oxidation than AMC1 over the entire evaluated temperature range. The mass variation at different temperatures was also similar for AMC4 and AMC3 [16], but higher mass losses were determined at 1200 and 1400 °C for the latter. The good resistance of AMC4 at the highest temperature is mainly attributed to the presence of Si [7], which forms mullite, as was determined by the analysis of the thermal evolution (Section 3.5).

It is worthy to note that the carbon present in AMC4 as graphite and glassy-C showed itself to be highly susceptible to oxidation, as can be observed in TGA thermograms of the three materials present in

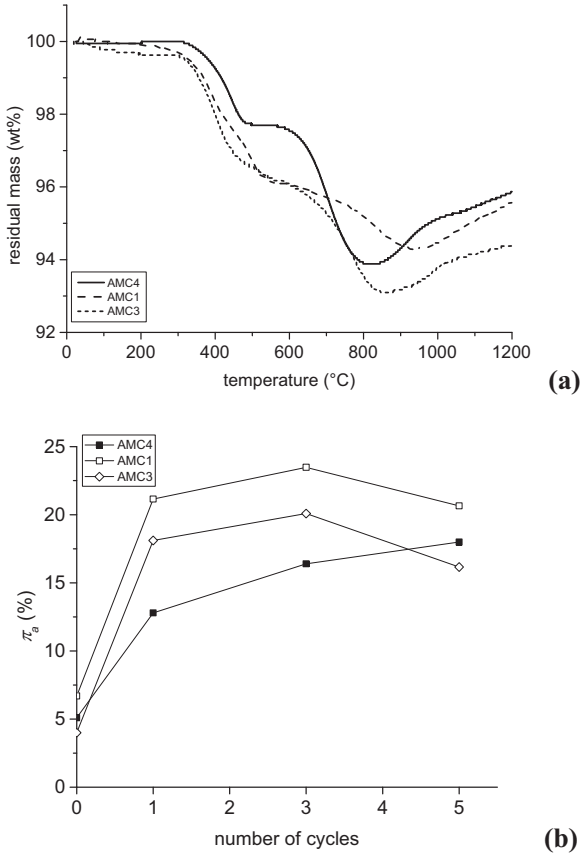

Fig. 19. Thermograms of the three original AMC bricks (a) and apparent porosity variation in function of the number of cycles in PLC testing at 1400 °C (b).

Fig. 19a: the temperature where the direct oxidation ends in AMC4 is lower than that in the other two materials. This was also confirmed by DTA: the maximum of the peak corresponding to carbon oxidation was 750 °C, 914 °C and 982 °C for AMC4, AMC1 and AMC3, respectively. This was mainly attributed to the characteristics of the graphite flakes in AMC4, mainly the smaller length and the lower aspect ratio; both factors reduce the inherent oxidation resistance of these particles [26]. An indicator of this attribute is the fact that graphite in AMC4 oxidizes together with the residual carbon formed from resin pyrolysis (Section 3.5), whereas this type of carbon reacts before graphite flakes in AMC1 and AMC3 [1,2]. Purity is another factor determining the oxidation behaviour of graphite flakes [26]; these particles are purer than those of AMC1 (> 94 wt%) but less so than the flakes present in AMC3 (> 97 wt%).

Considering the low resistance of the graphite flakes in AMC4, another factor to be considered to explain its good performance is the slightly low apparent porosity together with the high fraction of small pores, especially those < 1 μm, with these characteristics being the basis for inferring that the permeability of AMC4 is lower than that of AMC1 and AMC3. Moreover, the apparent porosity growth when the temperature increased was less for AMC4, as is observed in Fig. 19b for PLC testing, which increases the difference between this material and the other two refractories at high temperature.

Finally, the corrosion resistance to slag attack evaluated by static testing showed that AMC4 is now similar to AMC1, both exhibiting resistances higher than AMC3. Reasons for the difference between the corrosion behaviour of AMC1 and AMC3 at 1450 °C were previously discussed [16]: AMC1 has a greater amount of tabular alumina, which is the most chemical-resistant particle, and fine $MgAl_2O_4$ spinel is formed easily when the temperature increases. With respect to AMC1, AMC4 is in a similar situation as AMC3: it hasn't a high proportion of tabular alumina (and the quality of part of these particles is poorer) and the formation of spinel is the slowest (Fig. 18). Taking these facts into account, the similar corrosion resistance of AMC1 and AMC4 is attributed to the low permeability of the latter and the reduced growth of apparent porosity when the temperature is near 1450 °C (Fig. 19b). These textural characteristics probably counterbalance the poor contribution of the other two factors mentioned previously (content of tabular alumina and spinel formation), which are mainly responsible for the corrosion resistance of AMC1 against a basic slag melt at 1450 °C.

4. Conclusions

An analogous methodology previously proposed for the characterization of commercial AMC refractory bricks for steelmaking use, including a varied group of experimental and analytical techniques, were successfully applied to give an exhaustive description of a different AMC material containing aluminium and silicon as antioxidant additives. For this reason, some changes in the methodology should be done, and new techniques were also used, thus providing better descriptions of aspects which could not be analysed well before (for instance, granulometric characteristics). Moreover, a thermodynamic simulation analytical tool was also applied in this study.

A comparison with previously characterised AMC bricks containing only aluminium as an antioxidant, made it possible to explain the differences in thermal, oxidation and slag corrosion behaviour between the materials. The presence of silicon was linked to finer open porosity and a higher oxidation resistance at high temperature (1400 °C). In this case, these factors seemed to be more dominant than the oxidation resistance of the graphite flakes themselves. On the other hand, the degree of $MgAl_2O_4$ spinel formed was responsible for greater permanent linear change, especially when associated with finer particles, and also good corrosion resistance to the attack of a steelmaking ladle slag of basic character. However, special characteristics in the structure related to the ability to absorb volume changes also have an impact on the permanent linear change as well as low permeability, which is strongly related to pores sizes and has a significant influence on reducing the slag corrosion wear.

Acknowledgements

This work was supported by the Agencia Nacional de Promoción Científica y Tecnológica (ANPCyT) (PICT2006 No. 1887 and PICT2012 N.1215) of Argentina under projects "Degradación termoquímica y termomecánica de refractarios óxido-C de uso siderúrgico", PICT2006 No. 1887 and "Degradación química de refractarios de uso siderúrgico", PICT2012 No. 1215. The authors would like to thank Dr. P.G. Galliano for providing the material and participating in useful discussions, Mrs. M.L. Dignani for performing the permeability measurements, and Dra. E. Brandaleze for the opportunity to use the FactSage software.

References

[1] P. Ortega, M.J. Velasco, V. Muñoz, A.G. Tomba Martinez, P. Pena, Caracterización química y mineralógica de refractarios de Al_2O_3-MgO-C, Bol. Soc. Esp. Ceram. y Vidrio 51 (6) (2012) 305–312.

[2] V. Muñoz, M.P. Pena Castro, A.G. Tomba Martinez, Physical, chemical and thermal characterization of Al_2O_3-MgO-C refractories, Ceram. Int. 40 (2014) 9133–9149.

[3] P. Tassot, F. Etienne, J. Wang, P. Atkinson, New concepts for steel ladle linings, in: Proceedings of the Unified International Technical Conference on Refractories UNITECR'07, 2007, pp. 462–465.

[4] S. Chatterjee, R. Eswaran, Optimization of slag corrosion resistance and thermal expansion in Al_2O_3-MgO-C brick, in: Proceedings of the Unified International Technical Conference on Refractories UNITECR'09, 2009.

[5] C. Taffin, J. Poirier, The behaviour of metal additives in MgO–C and Al_2O_3–C refractories, Interceram 43 (1994) (354–358 (5)/458–460 (6)).

[6] S. Uchida, K. Ichikawa, K. Niihara, High-temperature properties of unburned MgO-C bricks containing Al and Si powders, J. Am. Ceram. Soc. 81 (22) (1998) 2910–2916.

[7] N.K. Ghosh, K.P. Jagannathan, D.N. Ghosh, Oxidation of magnesia-carbon refractories with addition of aluminium and silicon in air, Interceram 50 (3) (2001) 196–202.

[8] Z.A. Nemati, S.K. Sadrnezhaad, H.R. Ahamadi Mooghari, Effect of ferrosilicon, silicon and aluminium antioxidants on microstructures and mechanical properties of magnesia-graphite refractory, RA&N. 10 (6) (2005) 17–23.

[9] A.S. Gokce, C. Gurcan, S. Ozgen, S. Aydin, The effect of antioxidants on the oxidation behaviour of magnesia-carbon refractory bricks, Ceram. Int. 34 (2008) 323–330.

[10] A. Ghosh, S. Jena, H.S. Tripate, M.K. Haldar, V.P. Reddy, J. Ghosh, S.K. Das, A.K. Rama Rao, P. Ray, The influence of metallic antioxidants on some critical properties of magnesia-carbon refractories, Refract. WorldForm 5 (4) (2013) 69–74.

[11] R.K. Koley, K.A.V. Rao, S. Askar, S.K. Srivastava, Development and application of Al_2O_3-MgO-C refractory for secondary refining ladle, in: Proceedings of the Unified International Technical Conference on Refractories UNITECR'01, 2001.

[12] Y. Xu, Pore structure permeability, and alkali attack resistance of Al_2O_3-C concretes, Metall. Mater. Trans. A 45 (2014) 2885–2893.

[13] S. Shaobai, R. Bo, X. Yibio, L. Yawei, Improvement of gaseous corrosion resistance of refractories by pore structure design according to the seepage flow model, Refract. WorldForum 8 (3) (2016) 111–1117.

[14] DIN EN 993-1 (DIN 51056), Method of test for dense shaped refractory products. Determination of bulk density, apparent porosity and true porosity, 1995.

[15] ASTM C577-07, Standard Test Method for Permeability of Refractories, 2014.

[16] V. Muñoz, P.G. Galliano, E. Brandaleze, A.G. Tomba Martinez, Chemical degradation of commercial Al_2O_3-MgO-C refractory bricks by air and basic slag, J. Eur. Ceram. Soc. 35 (2015) 1621–1635.

[17] I.D. Kashcheev, V.P. Semyannikov, Role of structural factors in improving the corrosion resistance of refractories, Transl. Ogneup. (9) (1993) 2–4.

[18] C. Baudín, C. Alvarez, R.E. Moore, Influence of chemical reactions in magnesia – graphite refractories I. Effects on texture and high temperature mechanical properties, J. Am. Ceram. Soc. 82 (1999) 3529–3538.

[19] G. Buchebner, R. Neuboeck, S. Grassegger, Carbon-Bonding – a new milestone on low emission magnesia-carbon bricks, in: Proceedings of the Unified International Technical Conference on Refractories UNITECR'01, 2001.

[20] A. Watanabe, H. Takahashi, S. Takanaga, N. Goto, O. Matsuura, S. Yoshida, Thermal and mechanical properties of Al_2O_3-MgO-C bricks, Taikabutsu Overseas 10 (1990)

137–147.
[21] P. Williams, A. Hagni, Mineralogical studies of alumina magnesia carbon steel ladle refractories, in: Proceedings of the Unified International Technical Conference on Refractories UNITECR'97, 1997, 183–192.
[22] Y. Kiyota, Reduction of permanent linear change of Al_2O_3-MgO castable, in: Proceedings of the Unified International Technical Conference on Refractories UNITECR'07, 2007, pp. 546–549.
[23] A. Gardziella, J. Suren, M. Belsue, Carbon form phenolic resins: carbon yield and volatile components - recent studies, Interceram 41 (7/8) (1992) 461–467.
[24] L. Costa, L. Rossi di Montelera, G. Camino, E.D. Weil, E.M. Pearce, Structure-charring relationship in phenol-formaldehyde type resins, Polym. Degrad. Stab. 56 (1997) 23–35.
[25] S.K. Sadrnezhaad, S. Mahshid, B. Hasemi, Z.A. Nemati, Oxidation mechanism of C in MgO–C refractory bricks, J. Am. Ceram. Soc. 89 (4) (2006) 1308–1316.
[26] G.R. Doughty, L.S. Tovey, A comparison of the oxidation behaviour in air at 1050 °C of natural flake graphites, in: Proceedings of the Unified International Technical Conference on Refractories UNITECR'93, 1993, pp. 831–839.